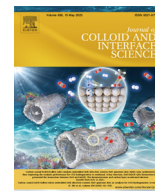




Contents lists available at ScienceDirect

Journal of Colloid and Interface Science

journal homepage: www.elsevier.com/locate/jcis

Direct growth of nano-worm-like Cu_2S on copper mesh as a hierarchical 3D catalyst for Fenton-like degradation of an imidazolium room-temperature ionic liquid in water

Xin-Yu Jiang^a, Eilhann Kwon^b, Jet-Chau Wen^c, Jorge Bedia^d, Bui Xuan Thanh^e, Suresh Ghotekar^f, Jechan Lee^{g,*}, Yu-Chih Tsai^a, Afshin Ebrahimi^{h,i}, Kun-Yi Andrew Lin^{a,*}

^a Department of Environmental Engineering & Innovation and Development Center of Sustainable Agriculture, National Chung Hsing University, Taichung 402, Taiwan

^b Department of Earth Resources and Environmental Engineering, Hanyang University, SeongDong-Gu, Seoul, Republic of Korea

^c National Yunlin University of Science and Technology, Douliu, Yunlin County, Taiwan

^d Chemical Engineering Department, Facultad de Ciencias, Universidad Autonoma de Madrid, Campus Cantoblanco, Madrid E-28049, Spain

^e Faculty of Environment and Natural Resources, Ho Chi Minh City University of Technology (HCMUT), Ho Chi Minh City 700000, Viet Nam

^f Department of Chemistry, Smt. Devkiba Mohansinhji Chauhan College of Commerce & Science, University of Mumbai, Silvassa 396 230, Dadra and Nagar Haveli (UT), India

^g Department of Global Smart City & School of Civil, Architectural Engineering, and Landscape Architecture, Sungkyunkwan University, Suwon 16419, Republic of Korea

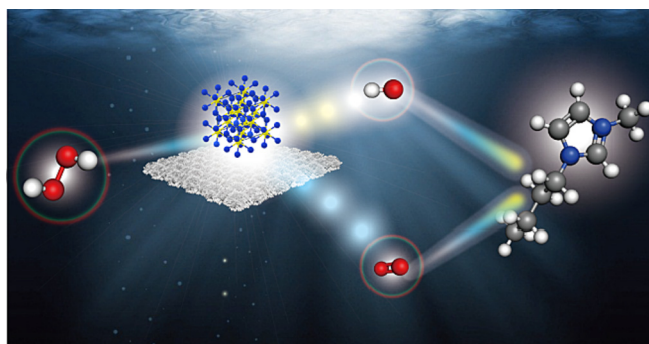
^h Department of Environmental Health Engineering, School of Health, Isfahan University of Medical Sciences, Isfahan, Iran

ⁱ Environment Research Center, Research Institute for Primordial Prevention of Non-Communicable Disease, Isfahan University of Medical Sciences, Isfahan, Iran

HIGHLIGHTS

- Nano-Worm-like Cu_2S is uniformly and well-dispersedly grown at Cu Mesh (CSCM).
- CSCM has the macroscale practicality as a mesh and the nanoscale functionality as nanoworms.
- Comparisons are made to investigate the structure–property relationship of CSCM.
- CSCM exhibits the more superior textural, electrochemical and catalytic properties.
- CSCM also enables a lower E_a of C4mim degradation than the reported activation energies.

GRAPHICAL ABSTRACT



ARTICLE INFO

Article history:

Received 10 November 2022

Revised 4 January 2023

Accepted 6 January 2023

Available online 8 January 2023

Keywords:

H_2O_2

Ionic liquids

Fenton

Cu_2S

Copper mesh

ABSTRACT

The increasing consumption of room-temperature ionic liquids (RTILs) inevitably releases RTILs into the water environment, posing serious threats to aquatic ecology due to the toxicities of RTILs. Thus, urgent needs are necessitated for developing useful processes for removing RTILs from water, and 1-butyl-3-methylimidazolium chloride (C4mimCl), the most common RTIL, would be the most representative RTIL for studying the removal of RTILs from water. As advanced oxidation processes with hydrogen peroxide (HP) are validated as useful approaches for eliminating emerging contaminants, developing advantageous heterogeneous catalysts for activating HP is the key to the successful degradation of C4mim. Herein, a hierarchical structure is fabricated by growing Cu_2S on copper mesh (CSCM) utilizing CM as a Cu source. Compared to its precursor, CuO@CM , this CSCM exhibited tremendously higher catalytic activity for catalyzing HP to degrade C4mim efficiently because CSCM exhibits much more superior electrochemical properties and reactive sites, allowing CSCM to degrade C4mim rapidly. CSCM also exhibits a smaller E_a of C4mim elimination than all values in the literature. CSCM also shows a high capacity and

* Corresponding authors.

E-mail addresses: jechanlee@skku.edu (J. Lee), linky@nchu.edu.tw (K.-Y.A. Lin).

stability for activating HP to degrade C4mim in the presence of NaCl and seawater. Besides, the mechanistic investigation of C4mim elimination by CSCM-activated HP has also been clarified and ascribed to OH and $^1\text{O}_2$. The elimination route could also be examined and disclosed in detail through the quantum computational chemistry, confirming that CSCM is a useful catalyst for catalyzing HP to degrade RTILs.

© 2023 Published by Elsevier Inc.

1. Introduction

Room-temperature ionic liquids (RTILs) represent a novel class of molten salts that can show liquid-like properties and behaviors at ambient temperature [1–3]. Since RTILs exhibit almost no vapor pressure at ambient conditions and superior thermal stability [4], RTILs have been broadly applied not only as green solvents but also as functional materials in biomass conversion, electrochemical applications, and energy production [1,2]. Unfortunately, increasing consumption of RTILs in various applications/processes has released RTILs into many water bodies [5], threatening the aquatic ecology and public health in view of the toxicities of RTILs [6]. Therefore, it is highly crucial to develop useful approaches for removing the RTILs from the contaminated water.

In general, RTILs can be classified into two major groups based on their cations: imidazolium and pyridinium. The relatively common imidazolium-based cations of RTILs include 1-ethyl-3-methyl-, 1-butyl-3-methyl-, and 1-octyl-3-methyl-, whereas the relatively popular pyridinium-based cations of RTILs include 4-methyl-*N*-butyl-pyridinium and *N*-octylpyridinium. In addition, tetraethylammonium and tetrabutylammonium both are also frequent cations comprised in RTILs.

Among all these RTILs, imidazolium (mim)-bearing RTILs are the most typical category [7–10]. These mim-based RTILs generally contain the imidazolate and R_4N^+ groups. Specifically, amidst numerous mim-based RTILs, 1-butyl-3-methylimidazolium chloride (C4mimCl) is the most common mim-based RTILs, which has been intensively studied as a representative RTIL [11–13]. Thus, it would be important and practical to develop efficient methods for treating C4mim-containing wastewater and eliminating C4mim from polluted water.

While a few approaches have been evaluated for removing C4mim, including sorption [14,15], filtration [16], as well as oxidation [11,17–24]. Oxidation appears as the most advantageous approach for removing C4mim as oxidation processes would decompose C4mim to reduce its negative impact [18,25]. To date, a number of oxidation processes have been proposed for degrading C4mim in water, such as Fenton's reaction [18,20–23] and electro-Fenton's process [17]. These processes are typically performed by the addition of hydrogen peroxide (HP) (i.e., H_2O_2) using homogeneous non-recyclable catalysts (i.e., Fe^{2+}) or high electricity demand, making these processes less practical. Therefore, it would be desirable for developing heterogeneous catalytic processes for activating HP to degrade C4mim. While metal nanoparticles (NPs) have received great attentions as heterogeneous catalysts for the activation of HP, NPs tend to agglomerate even in aqueous environments, thus decreasing their catalytic activities for the activation of HP [26–29]. Moreover, NPs are difficult for recover after applications, causing secondary pollutions. Therefore, it would be more practical to immobilize nanoscale catalysts on macroscale supports to create hierarchical catalysts, simultaneously possessing nanoscale functionality and macroscale convenience. Therefore, they appear as feasible and useful macroscale supports because metal meshes are robust and porous, enabling the growth of nanomaterials on their surfaces, and allowing fluids to go through conveniently [30,31]. Among various metallic meshes, copper (Cu) meshes (CMs) are common metal meshes at inexpen-

sive costs [32]. CM can also serve as a source of Cu, which would be further transformed into Cu-based catalysts for activating HP.

Thus, this study aims to develop a hierarchical composite catalyst based on CM for activating HP to degrade C4mim. In particular, since activation of HP involves redox behaviors of catalysts, Cu sulfides (i.e., Cu_2S) are particularly chosen as the Cu-based species to be grown directly on CM, forming a $\text{Cu}_2\text{S}@CM$ (CSCM) as Cu_2S has been validated to exhibit superior electrochemical properties [33,34]. More importantly, for maximizing the reactive surface, CM would be firstly oxidized to grow nanoneedles of Cu-oxide on CM (COCM), which would offer larger surfaces and useful precursors for growing Cu_2S . Interestingly, the resultant Cu_2S derived from the sulfidization of nanoneedles of Cu-oxide would remain on the CM surface but exhibit the worm-like nanostructure with porosities, making it an interesting hierarchical composite catalyst for activating HP to degrade C4mim. As almost no such nanoscale/macroscale composite catalyst has been developed for activating HP to degrade C4mim, this work would be the first to report such a hierarchical catalyst for degrading C4mim in water.

2. Experimental

2.1. Chemicals

All chemicals involved in this study were acquired commercially and used directly without purification. Potassium persulfate (ACS reagent, $\geq 99.0\%$), sodium hydroxide (reagent grade, $\geq 98\%$), sodium sulfide (Na_2S) ($\geq 98.0\%$), and hydrogen peroxide (HP) (i.e., H_2O_2 , 30%) were purchased from Sigma-Aldrich (USA). *tert*-butyl alcohol (TBA) (ACS reagent, $\geq 99.0\%$), 5,5-dimethyl-1-pyrroline *n*-oxide (DMPO) ($\geq 97.0\%$), 2,2,6,6-tetramethylpiperidine (TMP) ($\geq 99.0\%$), benzoquinone (BQ) (reagent grade, $\geq 98\%$), 1-Methyl-2-pyrrolidone (anhydrous, 99.5%), and sodium azide (NaN_3) (purum p.a., $\geq 99.0\%$ (T)) were purchased from Alfa Aesar (USA). Copper mesh (CM) was acquired from Maychun Enterprise Co. Ltd. (Taichung, Taiwan).

2.2. Preparation of $\text{Cu}_2\text{S}@Cu$ mesh

All chemicals used here were received from supplier and used with purification. Fabrication of CSCM is illustrated in Fig. 1 by firstly using CM as a support and a precursor of Cu, followed by the oxidation by persulfate, and subsequently, the sulfidization by Na_2S .

At start, a piece of Cu mesh (CM) was carved into a small piece (e.g., 20 mm \times 30 mm), which was pretreated by cleansing it with DI water and ethanol. Next, the piece of CM was immersed in 50 mL of an aqueous mixture of 2.5 M of NaOH and 0.125 M of potassium persulfate for 10 min to afford a Cu-oxide@CM (COCM). Subsequently, COCM was then immersed in an aqueous solution of 5 mM of Na_2S for 30 min for sulfidization of CM. The resultant modified CM was then dried in N_2 atmosphere at 150 °C to afford the product, $\text{Cu}_2\text{S}@CM$ (CSCM).

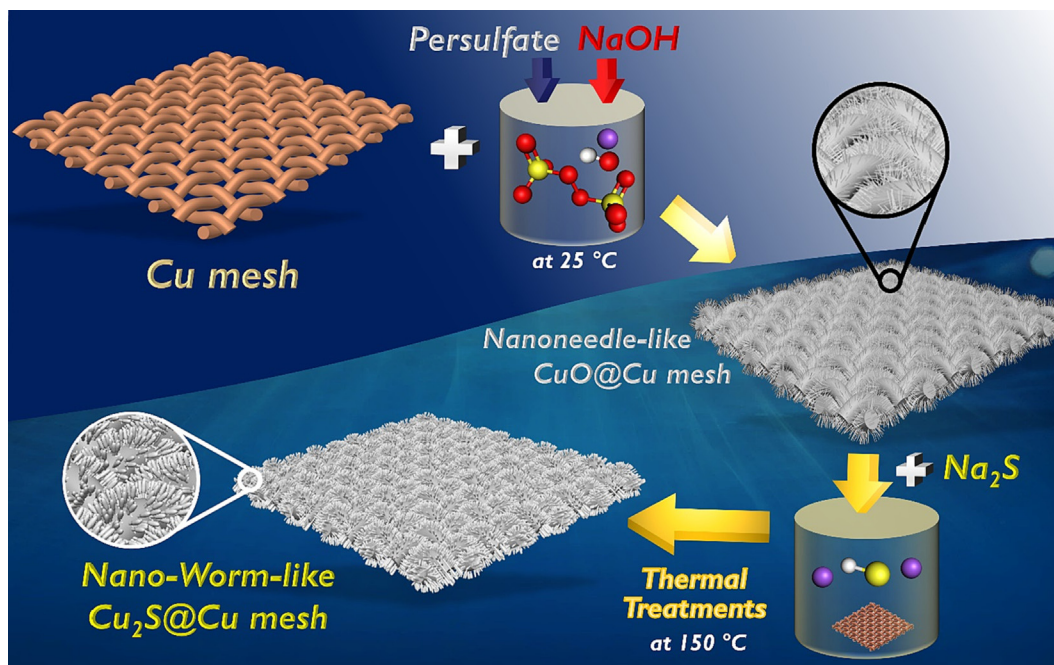


Fig. 1. Preparation scheme of $\text{Cu}_2\text{S}@$ Cu mesh (CSCM).

2.3. Characterization of catalysts

The appearance of all materials was determined using SEM (JEOL, Japan). Moreover, the crystalline structures of all as-prepared materials were characterized using an X-ray diffractometer (Bruker, USA). The surface chemistry of catalysts was further examined using X-ray photoelectron spectroscopy (XPS) (ULVAC-PHI, PHI 5000, Japan). The BET surface area and pore volume of catalysts were determined by N_2 sorption isotherms using a volumetric analyzer (Anton Paar Autosorb IQ, Austria). The electrochemical analysis was measured on an electrochemical workstation at room temperature using a standard three-electrode cell. A Pt wire as the counter electrode, an Ag/AgCl electrode as the reference electrode, and 20 μl of active suspension dropping on the glass carbon electrode was used as the working electrode. Dispersed 16 mg of catalysts, 2 mg of carbon black and 2 mg of polyvinylidene fluoride in 10 mL of 1-Methyl-2-pyrrolidone to form an active suspension. The electrolyte that can offer ions and assure the reversible chemical reaction was selected 1 M KOH (pH 13) or 0.5 M Na_2SO_4 (pH 6.6).

The cyclic voltammetry (CV) was operated at a scan rate of 60 mV s^{-1} in 1 M KOH solution. Using the 10 mV scan rate in 1 M KOH electrolyte to obtain the linear sweep voltammogram (LSV) curves. Applying a frequency from 10 Hz to 10000 Hz with a 5 mV amplitude to detect the electrochemical impedance spectroscopy (EIS).

2.4. Degradation of C4MIM using HP

C4mim degradation using HP (i.e., H_2O_2 solution) catalyzed by CSCM was evaluated by batch-type experiments. In a typical degradation experiment, 10 mM of HP was firstly added to a C4mim solution (0.2 L) with an initial concentration (C_0 of 5 mg/L). Next, A piece of CSCM (i.e., 60 mg) was hung, and immersed in the C4mim solution as displayed in Fig. S1 under visible light irradiation (150 W with a UV cut-off filter, Philips, Netherland). After preset intervals, sample aliquots were taken from the C4mim solution and then analyzed by HPLC (Kanuer Azura, Ger-

many) with a UV-Vis detector at 215 nm and a reverse-phase C-18 column to determine the residual concentration of C4mim (C_t). The mobile phase consists of DI water (35 %), methanol (64.9 %), and KH_2PO_4 (0.1 %) at a flowrate of 0.8 mL/min. Electron spin resonance (ESR) (Bruker, Germany) was employed to specify radical species generated from PDS. 5,5-Dimethyl-1-Pyrroline-*N*-Oxide (DMPO), and 2,2,6,6-Tetramethylpiperidine (TMP) were used as spin trapping reagents. The concentration of Cu found in the C4mim solution was determined using Inductively coupled plasma mass spectrometry (ICP-MS) (ICP-MS ELEMENT™ GD PLUS GD, ThermoFisher, USA). Error bars of data points would be calculated as the standard deviations of data points from two replicates of degradation experiments. The full information of computational investigations was detailed in the [supporting information](#).

3. Results and discussions

3.1. Characterization of catalysts

Morphology and composition

As the CM was employed as a support and a source of Cu, the pristine CM was also characterized in Fig. 2, and the surfaces of pristine CM were smooth without any specific structures (Fig. 2 (a-b)). The pristine CM exhibited a typical color of reddish brown as shown in Fig. 2(c). When the pristine CM was pretreated via the oxidation to afford a Cu-oxidize@Cu mesh (COCM), the resultant COCM showed a fluffy surface that was covered by fine needles as revealed in Fig. 2(d-f). The chemical composition of COCM by EDS analysis in Fig. 3(a) shows that this COCM consisted of only Cu and O without other elements. This indicates that surfaces on CM had been oxidized, and these needles might be nano-needles of Cu-oxide. Fig. 3(c) shows the crystalline structures of the pristine Cu mesh and the resultant COCM. While the pristine CM exhibited signature peaks at 43.4, 50.6 as well as 74.6°, attributed to the (111), (200), and (220) planes of Cu metal (JCPDS#03-1018), a number of additional peaks appeared after CM being oxidized by persulfate at 32.5, 35.4, 38.7, 38.9, and 73°, which were

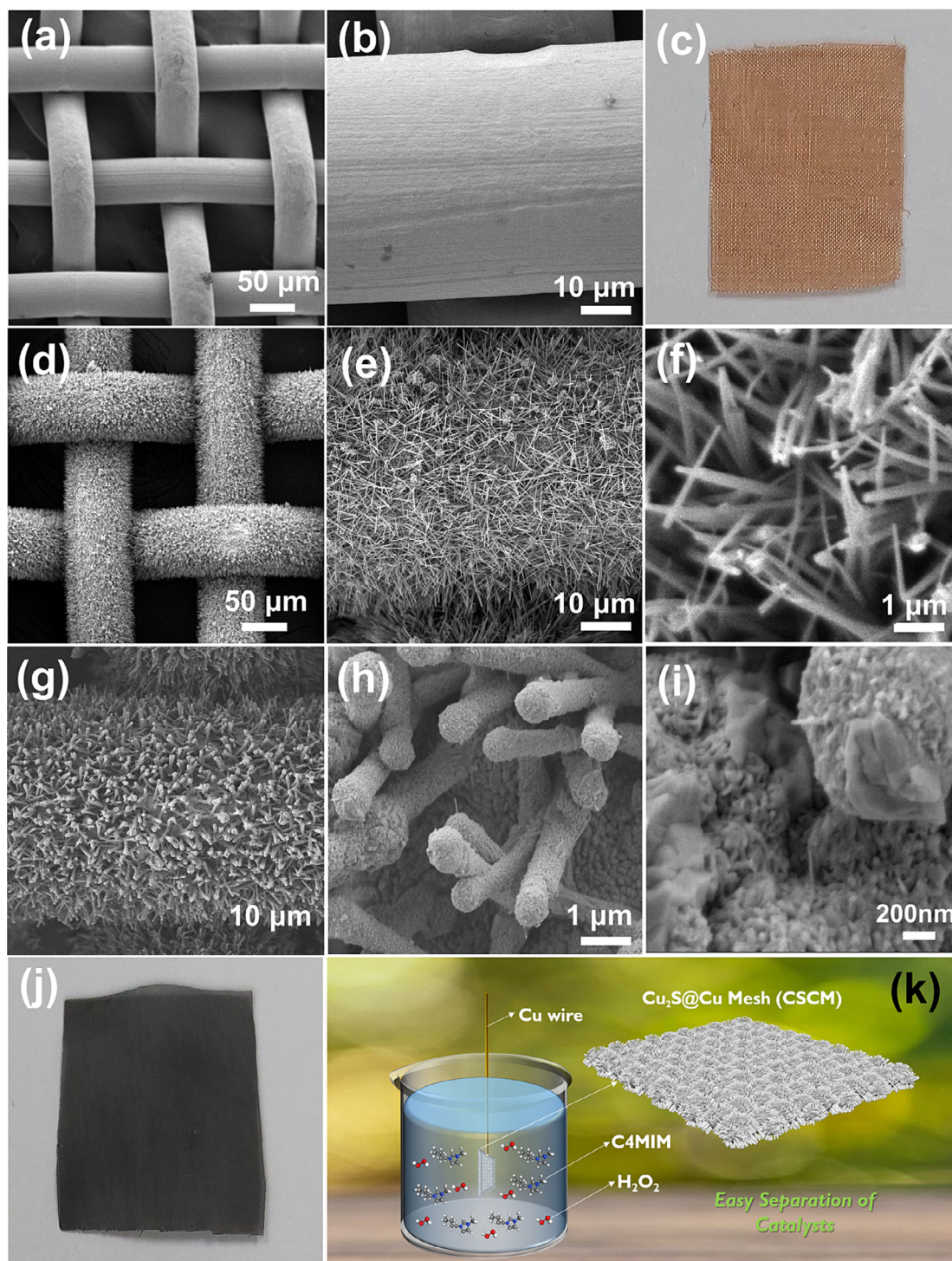


Fig. 2. SEM images and pictures of (a–c) pristine Cu mesh, (d–f) CuO@Cu mesh (COCM), (g–j) CSCM, and (k) illustration of suspending CSCM in the reaction medium.

well-indexed to the (110), (002), (111), (200), and (221) planes of CuO (JCPDS#48–1548) in Fig. 3(c).

Once this resulting COCM was further sulfidized by Na₂S, the mesh remained fluffy; however, the original nanoneedles became noticeably wider and thicker (Fig. 2(g)). The zoom-in image (Fig. 2(h)) displays that the nanoneedles of COCM had become nanoscale worm-like structures and the even-closer image (Fig. 2(i)) discloses that these nano-worm-like structures exhibited relatively coarse surfaces with the very fine pores on their surfaces. Fig. 2(j) further demonstrates this sulfidized CM which remained

as an intact piece of macrosized mesh. Thus, this resultant piece of sulfidized CM can be hanged by a Cu wire and suspended in the middle of the solution, as depicted in Fig. 2(k), allowing the solution to free flow through the mesh and then react with the active materials.

With this unique nano-worm structure with nanoscale pores grown on the macroscale mesh, this resulting composite material would exhibit the hierarchical structure, allowing it to exhibit a large reactive surface from its nanostructure and practicality as a macro-sized product. Perumal et al. reported the nano-worm-

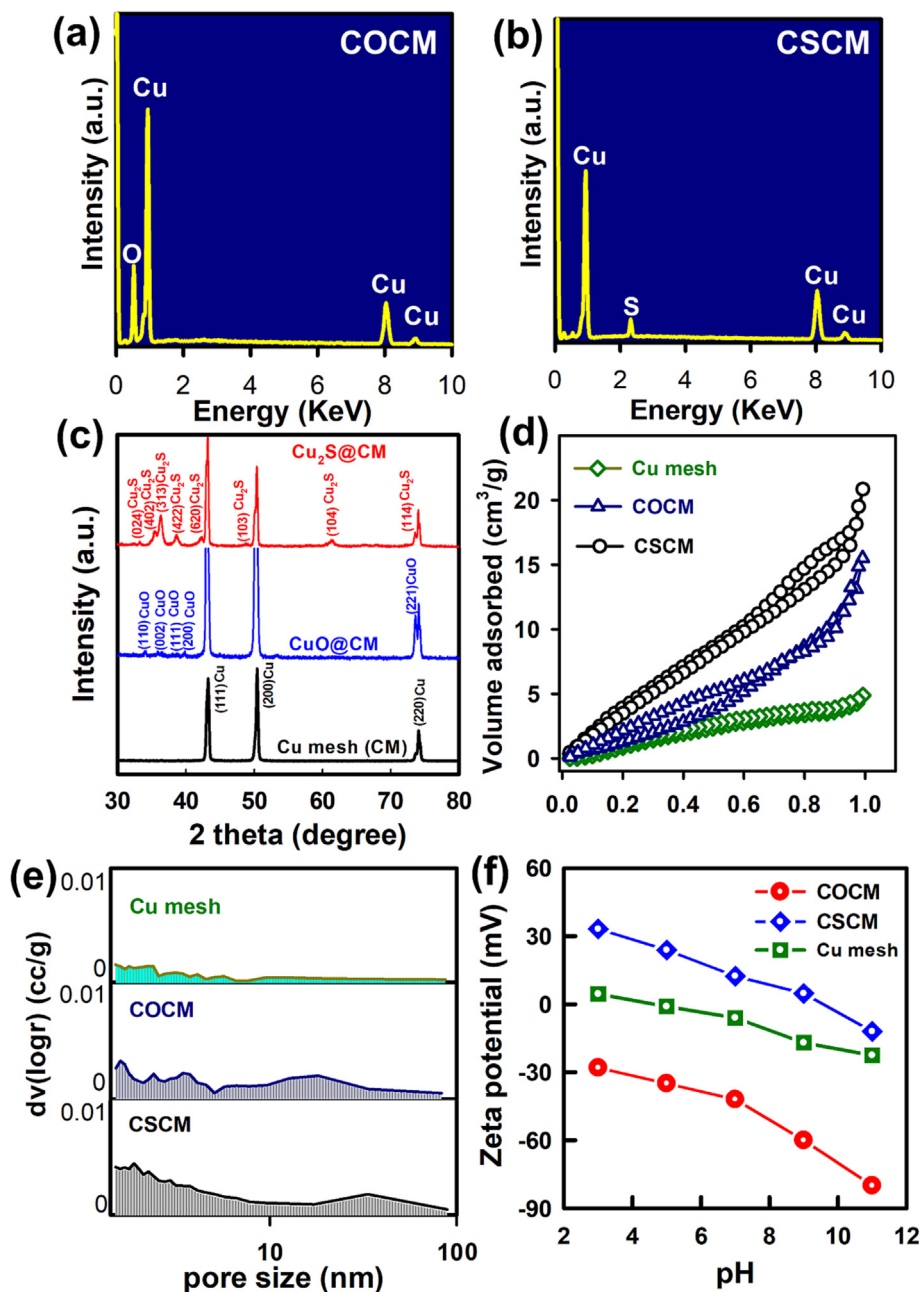


Fig. 3. (a) EDS of COCM; characterizations of CSCM: (b) EDS, (c) XRD, (d) N_2 sorption, and (e) pore sizes (f) zeta potentials.

like ZnO grown vertically from the thin film via the post-modification method by a hydrothermal process. Nevertheless, the resultant worm-like structures did not exhibit uniform morphologies and serious aggregates of the “worms” were also observed [35]. Additionally, Tao et al. reported the worm-like nanostructures by a nanoimprint lithography method, affording very high aspect-ratio nanoworms with a consistent size. Nonetheless, such nanoworm-like structures must be afforded via a highly-delicate protocol, which would be difficult to implement at a large scale [36].

Fig. 3(b) also unveils the composition of this unique composite material, which were comprised mainly of Cu, and S, indicating that these nanoworms on CM would be ascribed to copper sulfides. Fig. 3(c) further displays the corresponding crystalline structure of this sulfidized CM derived from COCM after the Na_2S treatment. Interestingly, most of CuO peaks were no longer present while

the peaks of CM itself still remained. More importantly, several noticeable peaks can be found at 33.1, 35.4, 36.5, 38.6, 42.4, 48.7, 61.3, and 73.8°, which would be well-indexed to the (024), (402), (313), (422), (620), (103), (104), and (114) planes of Cu_2S based on JCPDS Cards#33–0490 and 26–1116.

Fig. 4 further displays the distribution of elements in CSCM, and S and Cu would be uniformly spread over the substrate, signifying that CM had been successfully and uniformly transformed to CSCM. These characterizations also validated that the straightforward and relatively mild fabrication method can successfully convert the pristine CM into $Cu_2S@CM$ (CSCM) especially with the unique hierarchical structure. Xu et al. reported the growth of Cu_2S on a mesh via the direct sulfurization of Cu mesh [37]. However, the direct sulfurization of Cu mesh caused the inconsistent formation of Cu_2S , which then exhibited random configurations with the well-defined structures.

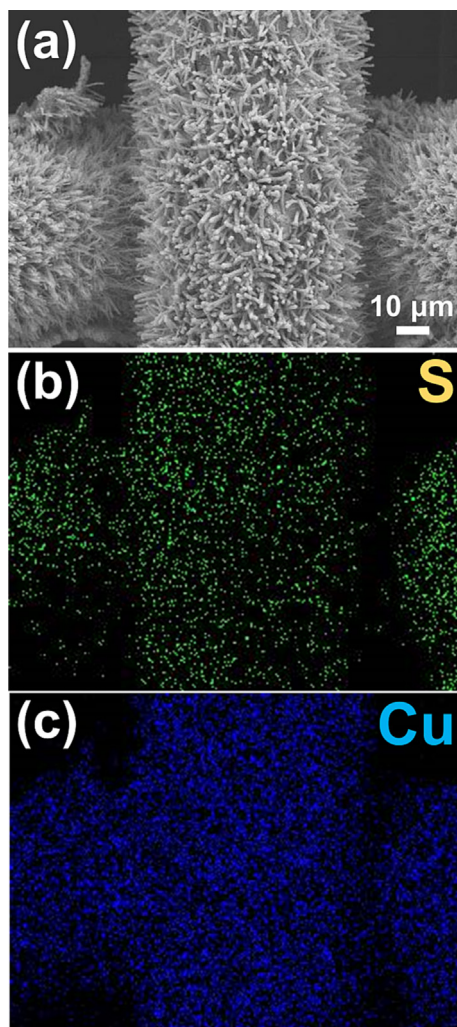


Fig. 4. Mapping analysis of CSCM: (a) Scanned region, (b) S, and (c) Cu.

4. Textural properties

Therefore, the textural properties of CSCM were further investigated by measuring its N_2 sorption isotherm as shown in Fig. 3(d). For comparisons, the N_2 sorption isotherms of COCM and the pristine CM were also measured and included in Fig. 3(d). The amount of N_2 sorption onto the pristine CM was relatively low because it exhibited very smooth surfaces and relatively few pores as displayed in Fig. 3(e); thus, the pristine CM merely possessed a specific surface area of $4.0 \text{ m}^2/\text{g}$ and a pore volume of $0.005 \text{ cm}^3/\text{g}$. After CM was oxidized and converted to COCM, its corresponding N_2 sorption was substantially increased, resulting in a higher specific surface area of $10.2 \text{ m}^2/\text{g}$. Its porous analysis is then displayed in Fig. 3(e), and the pore volumes of different sizes were all noticeably augmented, leading to a higher pore volume of $0.024 \text{ cm}^3/\text{g}$, possibly because those nanoneedles were bundled and inter-woven together, resulting in more pores. Once COCM was then sulfidized, affording CSCM, its N_2 sorption became even higher, resulting in an even higher surface area of $24.4 \text{ m}^2/\text{g}$, and the isotherm seemed to have a hysteresis loop, suggesting that the mesopores existed in CSCM. Its corresponding pore size distribution validated that a relatively large fraction of mesopores (i.e., $2 \sim 10 \text{ nm}$) can be found in CSCM, possibly owing to those fine voids present on the surface of the nano-worm-like structure of CSCM, leading to the even higher pore volume of $0.032 \text{ cm}^3/\text{g}$. These results confirm that CSCM pos-

essed a more favorable textural property than COCM and the pristine CM owing to its uniquely-shaped hierarchical and nano-worm-like structure.

5. Surface properties

Besides, as the degradation of C4mim and catalytic activation of HP would involve surficial interactions between C4mim, HP, and catalysts, surface properties, such as surface charges, might influence these interactions. Thus, the zeta potentials of COCM and CSCM at different pH were measured in Fig. 3(f). COCM exhibited a relatively positive charge of 33 mV at $\text{pH} = 3$, which gradually dropped at a higher pH and reached a negative charge of -15 mV at $\text{pH} = 11$. The tendency of COCM's surface charge as a function of pH was consistent with the literature [38]. On the other hand, the zeta potential of CSCM as a function of pH seemed noticeably different from that of COCM as the surface charges of CSCM were relatively negative. At $\text{pH} = 3$, its corresponding surface charge had been -30 mV , which would also continue to decrease and reach -80 mV at $\text{pH} = 11$. As C4mim is a cationic compound, the relatively negative surface of CSCM might benefit their interaction, improving degradation efficiency of C4mim by CSCM.

5.1. Degradation of C4mim by HP activation using different catalysts

At first, since C4mim might be removed by adsorption [14,15], it is essential to study if C4mim could be eradicated via sorption to catalysts. Fig. 5(a) displays that sorption of C4mim onto CSCM seemed marginal as only $\sim 5\%$ of C4mim ($C_t/C_0 = 0.95$ at 90 min) was removed by CSCM. On the other hand, HP alone was also tested to examine whether HP itself would eliminate C4mim. The C_t/C_0 reached 0.85 after 90 min possibly caused by certain reactive oxygen species (ROS) derived from the self-dissociation of HP. However, both CSCM and HP individually could not eliminate C4mim efficiently.

Next, once CSCM and HP were combined, and C4mim was rapidly eliminated, approaching to zero over 90 min. This result indicates that CSCM could catalyze HP to produce sufficient ROS for degrading C4mim. In comparison to CSCM, COCM was also tested for degrading C4mim; the concentration of C4mim also dropped noticeably in 90 min, suggesting that COCM was also capable of catalyzing HP for degrading C4mim. Nevertheless, the corresponding C_t/C_0 over 90 min merely approached 0.78. Besides, the C4mim degradation by COCM proceeded much more slowly than that by CSCM.

For further comparing the degradation kinetics of C4mim by CSCM and its precursor, COCM, the pseudo 1st order equation is employed here as follows

$$\ln\left(\frac{C_t}{C_0}\right) = -kt \quad (1)$$

where k represents the apparent pseudo 1st order rate constant (min^{-1}). The corresponding k values of C4mim by different methods are then calculated and summarized in Fig. 5(b). As CSCM and HP individually exhibited significantly low k values (i.e., 5×10^{-4} and $1.7 \times 10^{-3} \text{ min}^{-1}$, respectively), COCM certainly led to a higher k as $3.2 \times 10^{-3} \text{ min}^{-1}$. However, CSCM could exhibit an exceptionally higher k as $5.5 \times 10^{-2} \text{ min}^{-1}$, validating that CSCM showed a significantly higher catalytic activity than COCM for catalyzing HP to eliminate C4mim, and the sulfidization substantially boosted the catalytic activity of CM.

Since degradation of pollutants was essentially associated with ROS generated from catalytic activation of HP, heterogeneous catalysis of HP activation would be then attributed to electron-transfer behaviors, redox characteristics, and surficial properties

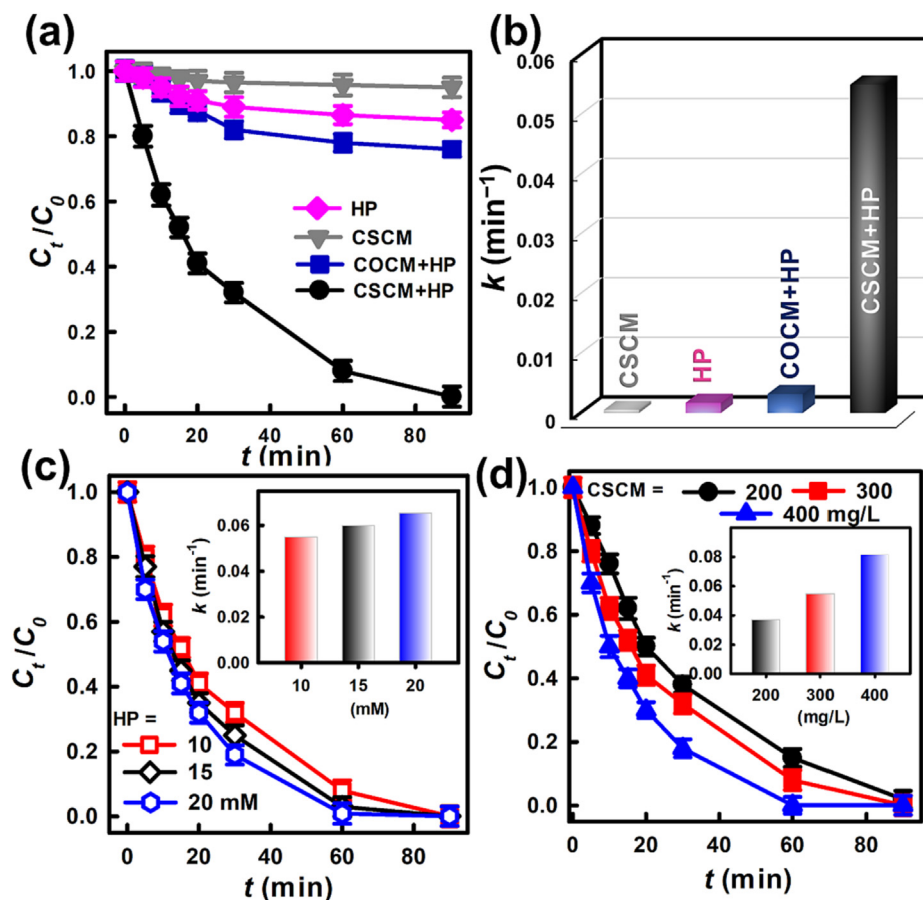


Fig. 5. (a) Comparison of degradation of C4mim and (b) corresponding rate constants by various catalysts; effects of (c) CSCM concentration (HP = 10 mM), and (d) HP concentration (HP = 200 mg/L, T = 30 °C) (Error bars: the standard deviations of data points from two replicates of degradation experiments).

of catalysts [39,40]. Thus, it was necessary to examine the electrochemical features of CSCM and COCM for clarifying the differences between COCM and CSCM, and the influence of the sulfidization.

Firstly, cyclic voltammetry (CV) curves of COCM and CSCM were obtained and shown in Fig. 6(a). CSCM exhibited the much more noticeable redox peaks and a larger current response than those of COCM, demonstrating that CSCM had superior redox properties than COCM. This also suggests that the interfacial reaction rates in CSCM would be much faster [41], thereby boosting catalytic activation of HP. This was also possible because CSCM possessed the

more surficial sites as well as porosity which would be larger ion basins [39,41], decreasing the diffusion length to the internal space and accelerating the ionic diffusion [42].

On the other hand, the linear sweep voltammograms (LSV) of COCM and CSCM were depicted in Fig. 6(b), and CSCM exhibited a considerably lower overpotential than COCM, signifying that the electron transport in CSCM was substantially enhanced. Moreover, for further comparing the active sites of COCM and CSCM, their scan rate-dependent CV curves in the non-Faradaic region with 1.0 M of KOH were measured in Fig. S1(a-b). The double layer

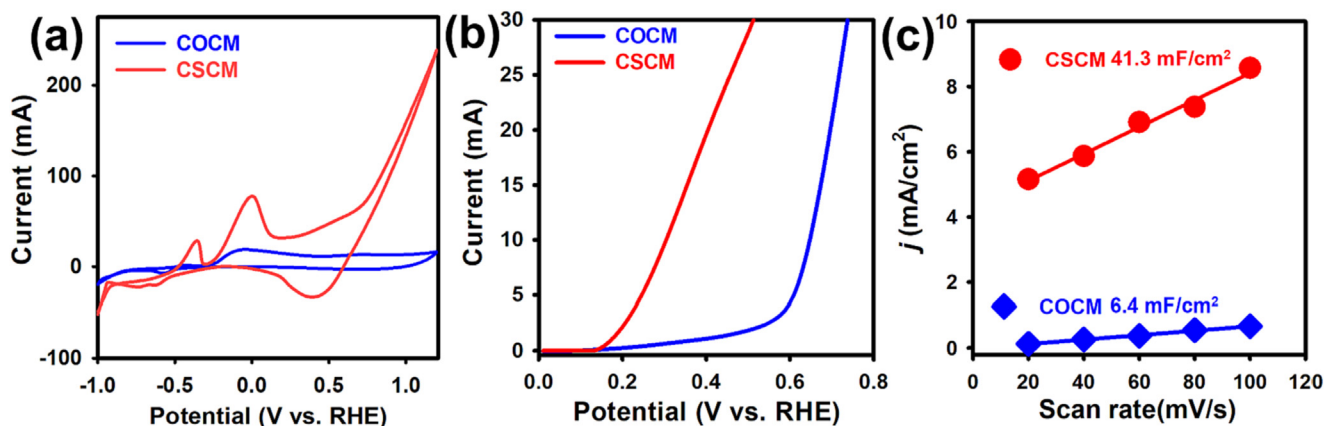


Fig. 6. (a) CV curves at a scan rate of 60 mV/s, (b) LSV curves, (c) ECSA of different catalysts.

capacitance (C_{DL}) would be quantified through the linear regression of J_m with v . The slopes of the linear fitting curves would be correlated to C_{DL} values of COCM and CSCM as shown in Fig. 6(c). CSCM exhibited a significantly higher C_{DL} value of 41.3 mF/cm² than 6.4 mF/cm² of COCM, suggesting that CSCM exhibited a higher active area of active sites than COCM. As CSCM possessed many superior electrochemical properties, it can exhibit a noticeably more superior performance for activating HP, and leading to the fastest rate constant of C4mim degradation. These analyses ascertained that the sulfidization of COCM into CSCM had tremendously improved the electrochemical properties, making CSCM a promising catalyst for HP activation.

In addition to the electrochemical properties, CSCM also exhibited the more superior textural characteristics than COCM with a higher specific surface area and pore volume, enabling CSCM to possess more active sites. Besides, since C4mim is a cationic compound and the surface charges of CSCM were much more negative than those of COCM, the electrostatic attraction between C4mim and CSCM seemed stronger than that between C4mim and COCM. These favorable features of CSCM might contribute simultaneously to the much higher C4mim degradation efficiency by CSCM in comparison with COCM.

5.2. Effects of CSCM and HP dosages on C4mim elimination

As the co-presence of CSCM and HP was found to degrade C4mim effectively, it would be useful to further evaluate the effects of CSCM and HP concentrations on C4mim degradation for elucidating their respective contributions to C4mim degradation.

Fig. 5(c) first displays C4mim degradation by varying HP from 10 to 30 mM with a constant dosage of CSCM as 300 mg/L. C4mim degradation was slightly affected at different HP dosages as a lower HP dosage of 10 mM led to the much slower degradation with a smaller $k = 5.5 \times 10^{-2} \text{ min}^{-1}$ even though C4mim could be still completely eliminated. Once HP became 15 mM, the C4mim degradation would be slightly enhanced as the k increased to $5.9 \times 10^{-2} \text{ min}^{-1}$. In the case of HP = 20 mM, C4mim could be completely eliminated at an even shorter time with a higher $k = 6.6 \times 10^{-2} \text{ min}^{-1}$. This demonstrates that the dosage of HP was critical as the availability of HP would greatly influence amounts of reactive oxygen species (ROS).

On the other hand, the dosage of CSCM was varied from 200 to 400 mg/L at a fixed concentration of 10 mM of HP. As CSCM at a relatively low concentration of 200 mg/L enabled the full elimination of C4mim in 90 min with a $k = 4.4 \times 10^{-2} \text{ min}^{-1}$ (see the inset in Fig. 5(d)), the higher dosages of CSCM at 300 and 400 mg/L would considerably expedite the full degradation of C4mim, reaching the k values of 5.5×10^{-2} and $8.1 \times 10^{-2} \text{ min}^{-1}$, respectively. A higher dosage of CSCM offers more reactive sites, thereby facilitating HP activation and enhancing C4mim degradation.

5.3. Other effects and reusability

5.3.1. Variation of temperature

To further explore the performance of CSCM, C4mim elimination would be tested at 30, 40, as well as 50 °C. Fig. 7(a) reveals that C4mim degradation using CSCM was substantially expedited at higher temperatures. Specifically, CSCM enabled the full degradation of C4mim rapidly at 30 °C with a k of $5.5 \times 10^{-2} \text{ min}^{-1}$, which then increased to $6.0 \times 10^{-2} \text{ min}^{-1}$ at 40 °C, and $6.8 \times 10^{-2} \text{ min}^{-1}$ at 50 °C. This demonstrates the positive influence of elevated temperatures on C4mim elimination.

Previous studies have also found that the relatively high temperatures (i.e., 70 ~ 90 °C) would enhance the degradation of C4mim by accelerating the kinetics and reducing the reaction time [21,22].

Moreover, as the k values of C4mim degradation became higher at the higher temperatures, the k value might be related mutually with temperature via the Arrhenius law:

$$\ln k - \ln A = -E_a/RT \quad (2)$$

The inset in Fig. 7(a) depicts a relationship between k and T . It can be appropriately fitted linearly with R^2 of 0.981, suggesting that the kinetics of C4mim degradation could be properly associated with temperature. On the other hand, the E_a value of C4mim degradation by CSCM + HP was computed as 8.6 kJ/mol, and it was tremendously lower than all the E_a values of C4mim elimination in literature, ranging from 23 to 43 kJ/mol, in Table 1, thereby ascertaining that CSCM would be an efficient catalyst for eliminating C4mim.

5.3.2. Effect of pH

In addition to temperature, the initial pH of the C4mim solution was also varied for examining the effect of pH especially as C4mim degradation by CSCM+HP is an aqueous reaction. Fig. 7(b) displays C4mim degradation by CSCM+HP at initial pH ranging from 3 to 11. As C4mim degradation under the neutral condition (i.e., pH = 7) was employed as a basis, the initial pH became relatively acidic at 5 seemed to make C4mim degradation proceed slower, and its corresponding k decreased from 5.5×10^{-2} to $1.7 \times 10^{-2} \text{ min}^{-1}$. Once initial pH was even lower at pH = 3, the corresponding k further decreased to $2.6 \times 10^{-3} \text{ min}^{-1}$. This was possibly because the abundant protons under the acidic condition might scavenge $\cdot\text{OH}$, thereby suppressing the C4mim degradation [46]. Besides, the acidic condition would make the CSCM surface less negatively-charged as shown in Fig. 3(f); thus, the electrostatic attraction between the cationic C4mim and CSCM might be lessened, thus causing the less efficacy of C4mim elimination.

Once pH became 9 under a relatively alkaline condition, the C4mim elimination would be also noticeably affected and proceeded slower than that under the neutral condition with a $k = 1.6 \times 10^{-2} \text{ min}^{-1}$. As the initial pH became even higher to 11, the C4mim degradation was also hugely interfered with, and the corresponding C_t/C_0 merely reached 0.8 with a very low k of $2.0 \times 10^{-3} \text{ min}^{-1}$. This was because the oxidation capability of HP is greatly associated with pH and its redox potential diminishes at increasing pH [47,48], leading to inefficient C4mim degradation.

This suggests that the most favorable environment for C4mim elimination by CSCM would be pH = 7; this feature is also reported in the literature for studying heterogeneous catalysis of HP in degrading contaminants, ascribed to the electrostatic interactions between contaminants and surface charges of catalysts [49].

5.3.3. Effects of NaCl, and types of different water sources

Aside from temperature and pH, the effect of co-existing ions might also influence C4mim degradation especially because C4mim was a cation, and it was added actually in the form of $[\text{C4mim}]^+[\text{Cl}]^-$, which consists of both a cation and an anion. To this end, NaCl is particularly chosen to represent the most common salt and a pair of cation/anion. In addition, wastewater also generally contains NaCl, which was then examined for its effect on C4mim degradation. Fig. 7(d) depicts C4mim elimination at different concentrations of NaCl. As C4mim could be fully and quickly eliminated by CSCM+HP in 90 min in the absence of NaCl, C4mim was still completely removed in 90 min with a $k = 5.1 \times 10^{-2} \text{ min}^{-1}$ in the presence of NaCl at 5 mg/L, which was the same mass concentration of C4mim in the solution. This indicates that when NaCl at an equivalent concentration of C4mim was present, the influence of NaCl on C4mim degradation was negligible. When the NaCl concentration increased to 50 mg/L, C4mim was also rapidly degraded, and the corresponding C_t/C_0 reached zero in 90 min with a k of $3.8 \times 10^{-2} \text{ min}^{-1}$. Even though NaCl was at

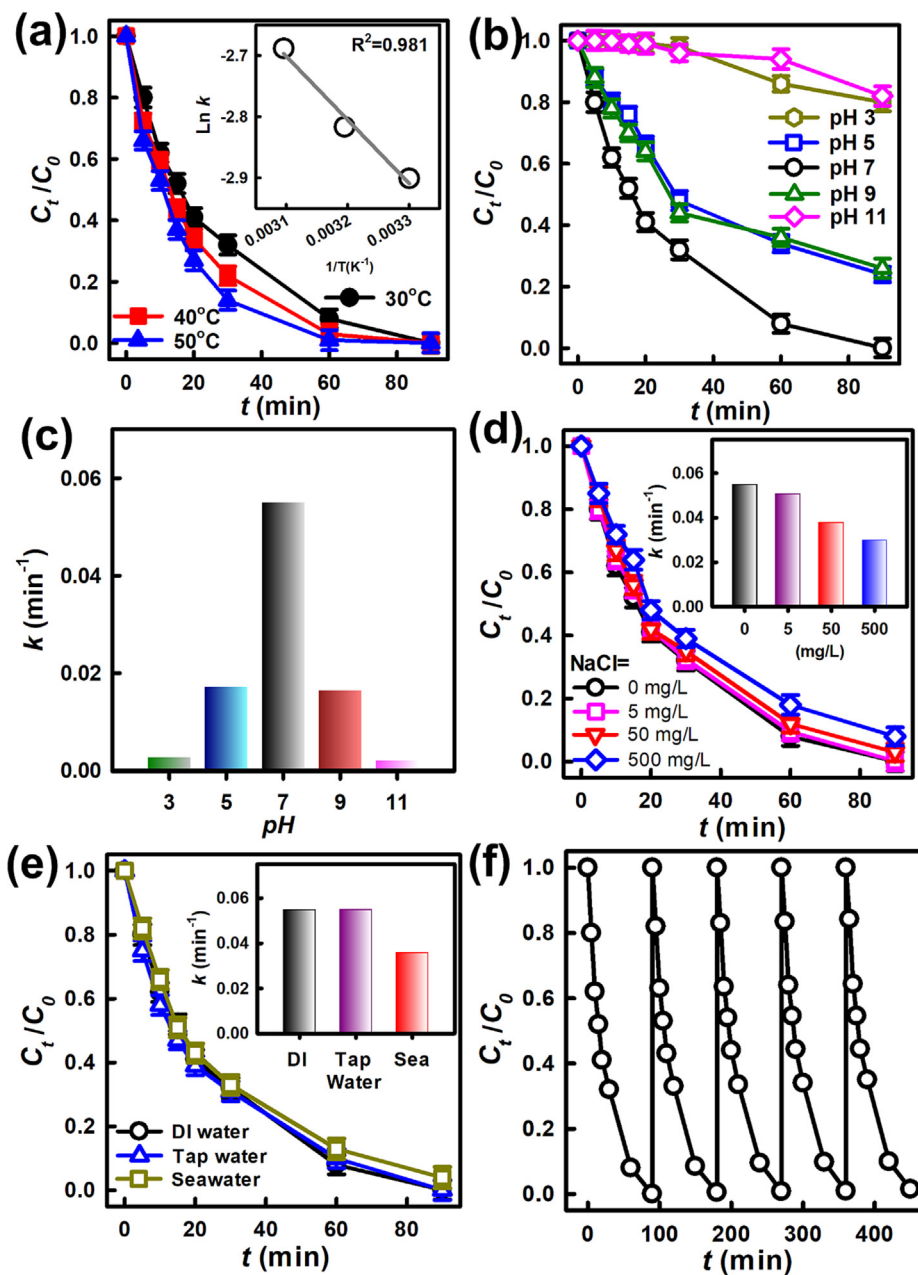


Fig. 7. Effects of (a) temperature, (b, c) pH, and (d) recyclability; (e) NaCl, and (f) water types (catalyst = 300 mg/L; HP = 10 mM/L; T = 30 °C) (Error bars: the standard deviations of data points from two replicates of degradation experiments).

Table 1
A comparison of E_a values for C4mim degradation*.

| Material / Oxidant | E_a (kJ/mol) | Reference |
|--|----------------|------------------|
| CSCM / H ₂ O ₂ | 8.6 | This work |
| FeNiC / persulfate | 40.4 | [43] |
| Fe ²⁺ / H ₂ O ₂ | 43.3 | [44] |
| Co ₃ O ₄ / Oxone | 23.9 | [45] |

* E_a calculated by the two replicate experiments at different temperatures.

a significantly high concentration of 500 mg/L, more than 90% of C4mim could be still eliminated in 90 min with a k of $3.0 \times 10^{-2} \text{ min}^{-1}$.

Furthermore, other types of water sources were also examined to probe into the influence of different water matrices on C4mim degradation by CSCM. As the DI water was employed as a basis,

C4mim in the tap water could be still quickly and effectually degraded as its corresponding k remained almost the same (i.e., $k = 5.5 \times 10^{-2} \text{ min}^{-1}$). This indicates that even though the tap water also contains some ions and molecules, C4mim could be still efficiently eliminated by CSCM. Interestingly, in the case of seawater, the C4mim degradation was slightly affected as more than 95% of C4mim was still eliminated with a $k = 3.6 \times 10^{-2} \text{ min}^{-1}$.

These results indicate that C4mim could be still efficiently degraded by CSCM+HP even with NaCl or different water matrices, revealing that CSCM would be a promising/practical catalyst for C4mim elimination via activation of HP.

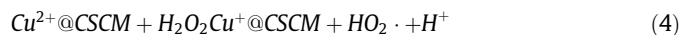
5.3.4. Reusability of CSCM, and activation mechanism of CSCM for HP

In addition to the aforementioned effects, the reusability of a heterogeneous catalyst is also crucial. Therefore, the reusability of CSCM was then examined by using CSCM over 5 consecutive

cycles. Fig. 7(f) displays that the spent CSCM was still capable of activating HP to degrade C4mim, and no significant loss of catalytic activity could be observed, demonstrating the high reusability of CSCM. On the other hand, the Cu concentration in the solution in the end of the recyclability experiment of C4mim degradation was measured to study if Cu was leached out, and dissolved in water. Nonetheless, the Cu concentration in the solution at the end of the recyclability test was detected as 0.003 mg/L by inductively coupled plasma mass spectrometry, which was much smaller than the original concentration of CSCM (i.e., 300 mg/L), suggesting that CSCM was a stable and robust catalyst.

Besides, the surface chemistry of CSCM using X-ray photoelectron spectroscopy before and after the recyclability was analyzed, and the core-level Cu and S spectra of CSCM were measured and displayed in Fig. 8. Specifically, the Cu2p spectrum of the pristine CSCM (Fig. 8(a)) can be deconvoluted to show numerous notable peaks at 934.0, 935.9, 941.6, 944.0, 953.8, 955.8, and 962.5 eV. Specifically, the peaks at 934.0 and 953.8 eV corresponded to Cu^+ , while the peaks at 935.9 as well as 955.8 eV were ascribed to Cu^{2+} [50]. Besides, the S2p spectrum (Fig. 8(b)) would be also deconvoluted to afford the dual bands at 162.0, and 163.1 eV, attributed to $\text{S}2\text{p}_{3/2}$ and $\text{S}2\text{p}_{1/2}$, respectively [51]. On the other hand, the spent CSCM from the recyclability test had been also analyzed, and its Cu2p and S2p spectra can be viewed in Fig. 8(c-d). Generally, the Cu2p and S2p spectra of CSCM were similar to those of the pristine CSCM, indicating that HP activation and C4mim degradation did not destroy CSCM. Nonetheless, the fractions of

Cu species before and after the recyclability test were slightly changed. The fraction of Cu^{2+} seemed smaller in the spent CSCM, whereas the fraction of Cu^+ would also become relatively high in the spent CSCM. These variations were consistent to the reported mechanism of HP activation, in which metal species would catalyze HP activation via the transformation of valence states of metal species through the following equations [52]:



Thus, this confirmed that C4mim elimination by CSCM + HP might be ascribed to the redox process of metal species in CSCM (i.e., $\text{Cu}^+/\text{Cu}^{2+}$). However, the fraction of S species in CSCM before and after the recyclability did not significantly change, suggesting that S species played a relatively minor role in activating HP by CSCM.

5.4. Mechanistic insights into C4mim elimination

For further study of the mechanism for HP activation by CSCM in C4mim degradation, two special radical scavengers were employed to examine ROS generated from CSCM-activated HP. Firstly, *tert*-butanol (TBA), consisting of no α -hydrogen, has been frequently employed as a probing agent for hydroxyl radical. Fig. 9(a) demonstrates that the addition of TBA would lead to a noticeable inhibition to C4mim degradation by CSCM as the corre-

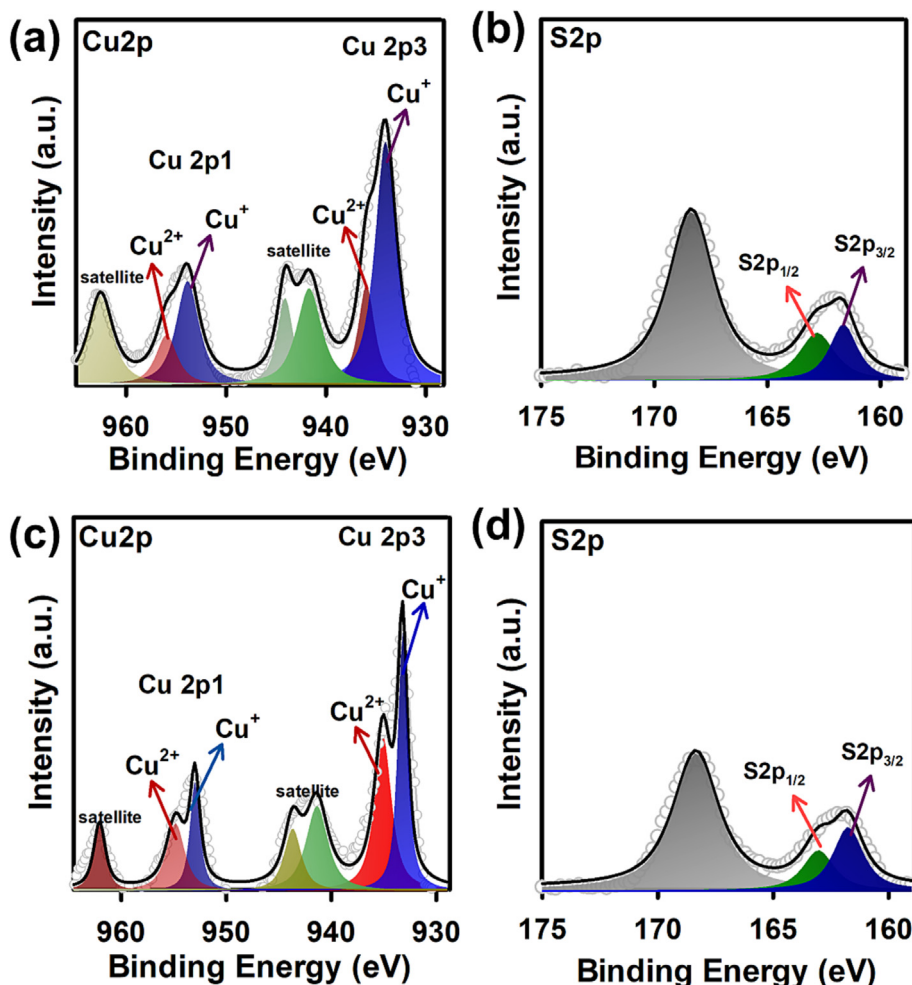


Fig. 8. XPS of (a-b) the pristine CSCM and (c-d) the used CSCM.

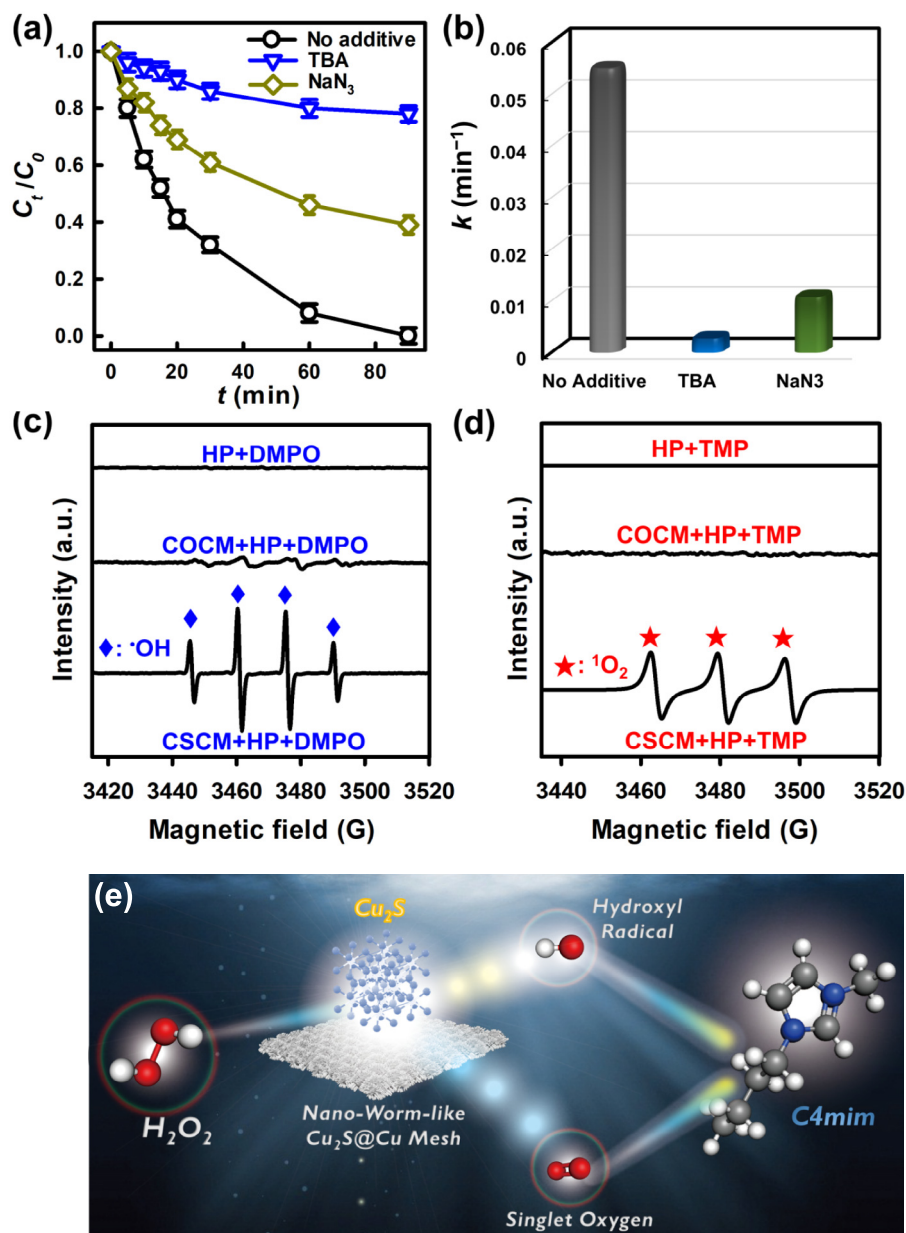


Fig. 9. Effects of radical probe on degradation of C4mim by CSCM: (a) degradation results (Error bars: the standard deviations of data points from two replicates of degradation experiments), (b) rate constants. ESR analyses: (c) DMPO, (d) TMP (catalyst = 300 mg/L; HP = 10 mM; T = 30 °C); (e) illustration of C4mim degradation by CSCM + HP.

sponding k became much smaller from originally 5.5×10^{-2} to $2.7 \times 10^{-3} \text{ min}^{-1}$ (Fig. 9(b)), signifying that $\cdot\text{OH}$ shall be involved during C4mim degradation.

On the other hand, as the decomposition of HP might also induce the formation of a non-radical ROS, singlet oxygen ($^1\text{O}_2$) [53,54], NaN_3 was then chosen as a probe agent for examining the presence of $^1\text{O}_2$. Fig. 9(a) reveals that C4mim degradation by CSCM would be also noticeably affected because k decreased to $1.1 \times 10^{-2} \text{ min}^{-1}$, and thus $^1\text{O}_2$ might be present in C4mim degradation. Previous studies indicate that Cu^{2+} might react with $\text{HO}_2\cdot$, which was produced according to Eq.(5) to result in the singlet oxygen as follows:



Moreover, electron spin resonance (ESR) spectroscopy was then adopted to analyze ROS generated from CSCM-activated HP. Initially, 5,5-Dimethyl-1-pyrroline *N*-Oxide (DMPO) was employed

as the spin-trapping agent, and no noticeable signal could be found from the combination of DMPO and HP (Fig. 9(c)). Once DMPO, CSCM and HP were simultaneously combined, the distinct pattern of DMPO-OH with a 1:2:2:1 quadruplet signal was obtained [53,55], validating the presence of $\cdot\text{OH}$. On the other hand, Fig. 9 (c) also displays the ESR result of the combination of DMPO, COCM and HP; a very weak signal of the adduct of DMPO-OH could be observed. This also indicates that the catalytic activity of COCM for catalyzing conversion of HP to $\cdot\text{OH}$ would be much lower than that of CSCM; thus, CSCM enabled a significantly more effective C4mim degradation than COCM.

On the other hand, 2,2,6,6-Tetramethylpiperidine (TMP) was also employed as the spin-trapping agent for identifying the existence of $^1\text{O}_2$. As no obvious signal was detected by HP alone (Fig. 9(d)), a distinct pattern of TMPO with a triplet signal was found in the mixture of TMP, HP and CSCM, confirming the presence of $^1\text{O}_2$ derived from HP. Nevertheless, when TMP, HP and

COCM were all mixed together, the corresponding ESR result (Fig. 8 (d)) did not reveal significant patterns, suggesting that COCM-induced production of $^1\text{O}_2$ was very insignificant.

These results demonstrate that C4mim degradation by CSCM-activated HP can be attributed to both $\cdot\text{OH}$ and $^1\text{O}_2$, which might be the reason that CSCM-activated HP can enable the highly-effective C4mim degradation, while C4mim degradation by COCM-activated HP was inefficient due to the very low quantity of $\cdot\text{OH}$ without other useful ROS.

5.5. Computational calculation and possible C4mim degradation pathway

With the advance of the quantum chemistry computation, reaction pathways, kinetics as well as regioselectivity of organic contaminants could be predicted and estimated to offer valuable information for design and operation of advanced oxidation processes [56,57]. As C4mim was efficiently degraded by CSCM-activated HP, it would be valuable to further explore the decomposition pathway of C4mim. Herein, the density functional theory (DFT) computation was particularly employed to offer insights into the susceptibility of possible reactive sites of C4mim given its

molecular orbitals (MOs) and the Fukui indices. Fig. 10(a) firstly displays the optimized structure of C4mim with its highest occupied MO (HOMO) in Fig. 10(c), and the lowest unoccupied MO (LUMO). The yellowish, and blueish areas of HOMO and LUMO represent the electron-deficient and electron-abundant regions of C4mim, respectively. The HOMO on the imidazolate ring has the tendency for releasing electrons; therefore, C4mim could be attacked by the electrophilic ROS, such $\cdot\text{OH}$. In addition, the electrostatic potential (ESP)-mapped analysis of C4mim (Fig. 10(b)) also suggests that the sites close to the imidazole ring would also attract the attack from ROS.

On the other hand, the Fukui indices of C4mim were also calculated, and summarized in Fig. 10(e) with the mapped isosurfaces of f^- , f^0 , and f^+ values in Fig. 10(f), (g) and (h), respectively. Generally, an atom with a large value of the Fukui index signifies a higher possibility for this atom to receive attacks. In particular, an atom with a large f^- value could be more easily attacked; thus, 6C, exhibiting the higher f^- , would be the most possible site for receiving attacks. Additionally, 2C, and 3C also exhibited the relatively high f^- values; thus, these atoms might also easily receive attacks in the beginning of C4mim degradation. Moreover, Fig. 10 (e), and (g) also reveal f^0 indices for determining probable atoms

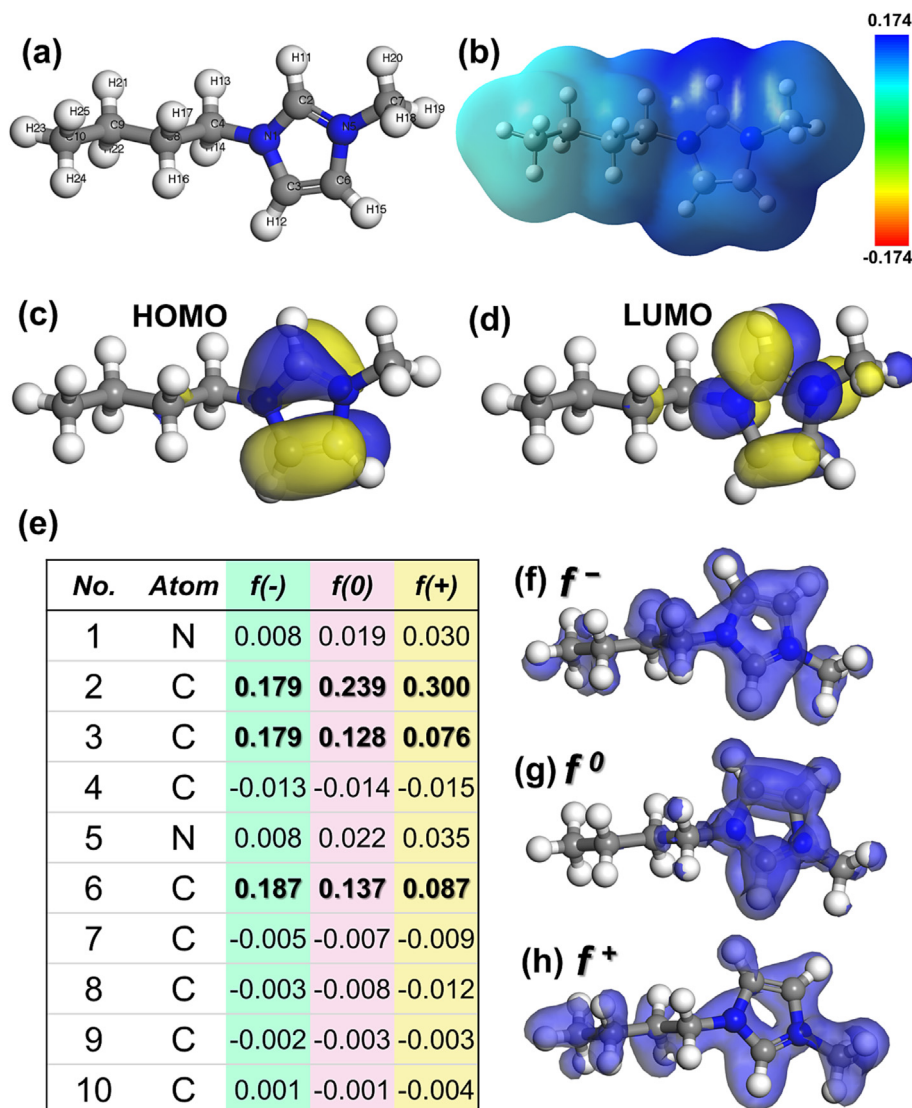


Fig. 10. DFT calculation for C4mim: (a) the optimized molecule structure; (b) electrostatic potential (ESP); (c) HOMO; (d) LUMO; and (e) the calculated condensed Fukui index distribution for electrophilic attack (f^-), radical attack (f^0), and nucleophilic attack (f^+).

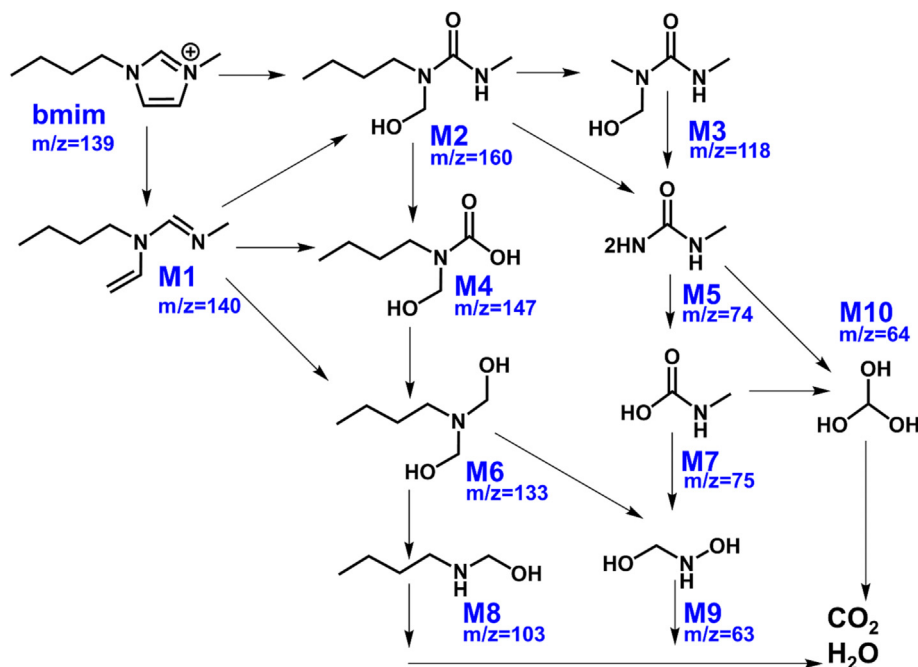


Fig. 11. A proposed degradation process of C4mim by CSCM + HP based on the detected intermediates.

for receiving non-radical attacks. 2C with the highest value of f^0 might be the most possible atom for receiving the non-radical attacks, followed by 6C and 3C. In view of these above-mentioned analyses, the C4mim degradation might be initiated by the attacks on the imidazolium ring at the possible sites of 6C, 2C and 3C.

For further determining the decomposition pathway of C4mim, the decomposition of C4mim by CSCM-activated HP would be then analyzed by mass spectrometry as displayed in Fig. S2, and the detected intermediates are summarized in Table S1. Given these molecules and insights from the DFT-assisted analyses, a possible decomposition pathway for C4mim by CSCM-activated HP could be depicted in Fig. 11 [17,18,58].

Initially, C4mim might be attacked at its imidazolium ring, which was then opened to become M1. Subsequently, M1 ((*E*)-*N*-butyl-*N'*-methyl-*N*-vinylformimidamide) might undergo further attacks to afford a series of by-products from the ring-open reaction, such as M2 (1-butyl-1-(hydroxymethyl)-3-methylurea), M4 (butyl(hydroxymethyl)carbamic acid) and M6 ((butylazanediy) dimethanol). In particular, M2 might be further decomposed to become M3 (1-(hydroxymethyl)-1,3-dimethylurea) and then M5 (1-methylurea) by eliminating the long alkyl chain of M2. The resulting M5 could be further oxidized and decomposed to generate M7 (methylcarbamic acid) as well as M10 (methanetriol). On the other hand, M4 might be also transformed to M6, which would be further decomposed to produce M8 ((butylamino)methanol), and subsequently, M9 ((hydroxyamino)methanol). These low-molecular-weight by-products (i.e., M8, M9, and M10) could be further oxidized and then broken down eventually to CO₂ and H₂O.

6. Conclusions

In this study, a hierarchically-structured Cu₂S grown on copper mesh (CM) can be afforded by directly employing CM as a template and precursor. Via the first-step oxidation, the high-aspect-ratio nanoneedles of CuO could be produced and protruded from the CM surface, affording large contact surface areas. The subsequent second-step sulfidization further transformed these nanoneedles

into relatively chubby worm-like structures. Especially, these nano-worms also exhibited highly porous surfaces as they were uniformly and densely grown on the macro-porous CM, making the resultant material a unique and versatile composite. These features enable this resulting Cu₂S@copper mesh (CSCM) to exhibit the much more superior textural, and electrochemical properties than the conventional non-sulfidized CuO@copper mesh, making CSCM show a significantly higher catalytic activity for activating hydrogen peroxide (HP) to degrade C4mim. These results validate that the proposed sulfidization treatment represents an efficient and promising protocol for boosting Cu-based catalyst; more importantly, such a CSCM also provided a much more practical and convenient route than the conventional powdered forms of catalysts for C4mim degradation in view of ease of recovery and separation of CSCM from solutions and robust recyclability. Moreover, CSCM with HP also led to a tremendously lower activation energy of C4mim degradation (8.6 kJ/mol) in comparison to other powdered and homogeneous catalysts (i.e., 23 ~ 43 kJ/mol), confirming that CSCM is not only practically useful but also highly efficient as CSCM can induce both radical and non-radical attacks on C4mim. This study successfully demonstrates the convenient technique for fabricating the hierarchically-structured Cu₂S grown on CM with the special worm-like and highly-porous configuration, providing insights for designing hetero-interfaced composites with superior textural properties to boost the surficial chemical properties in catalytic applications.

CRedit authorship contribution statement

Xin-Yu Jiang: Data curation, Writing – original draft. **Eilhann Kwon:** Data curation, Writing – original draft. **Jet-Chau Wen:** Data curation. **Jorge Bedia:** Data curation, Visualization, Investigation. **Bui Xuan Thanh:** Data curation. **Suresh Ghotekar:** Data curation, Visualization, Investigation. **Jechan Lee:** Data curation, Writing – original draft. **Yu-Chih Tsai:** Data curation, Visualization. **Afshin Ebrahimi:** Writing – review & editing. **Kun-Yi Andrew Lin:** Data curation, Writing – original draft.

Data availability

The authors are unable or have chosen not to specify which data has been used.

Declaration of Competing Interest

The authors declare that they have no known competing financial interests or personal relationships that could have appeared to influence the work reported in this paper.

Acknowledgement

This work is supported by the National Science and Technology Council (NSTC-112-2636-E-005-003), Taiwan, and financially supported by the “Innovation and Development Center of Sustainable Agriculture” from The Featured Areas Research Center Program within the framework of the Higher Education Sprout Project by the Ministry of Education (MOE), Taiwan. The authors gratefully acknowledge the use of SQUID000200 of MOST111-2731-M-006-001 belonging to the Core Facility Center of National Cheng Kung University.

Appendix A. Supplementary data

Supplementary data to this article can be found online at <https://doi.org/10.1016/j.jcis.2023.01.029>.

References

- H. Olivier-Bourbigou, L. Magna, D. Morvan, Ionic liquids and catalysis: Recent progress from knowledge to applications, *Appl. Catal. A* 373 (2010) 1–56.
- A.P.M. Tavares, B. Pinho, O. Rodriguez, E.A. Macedo, Biocatalysis in Ionic Liquid: Degradation of Phenol by Laccase, *Proc. Eng.* 42 (2012) 226–230.
- Introduction: Ionic Liquids, *Chem. Rev.* 117 (2017) 6633–6635.
- K.-Y.-A. Lin, A.-H.-A. Park, Effects of Bonding Types and Functional Groups on CO₂ Capture using Novel Multiphase Systems of Liquid-like Nanoparticle Organic Hybrid Materials, *Environ. Sci. Technol.* 45 (2011) 6633–6639.
- A. Oskarsson, M.C. Wright, Ionic Liquids: New Emerging Pollutants, Similarities with Perfluorinated Alkyl Substances (PFASs), *Environ. Sci. Technol.* 53 (2019) 10539–10541.
- T.P. Thuy Pham, C.-W. Cho, Y.-S. Yun, Environmental fate and toxicity of ionic liquids: A review, *Water Res.* 44 (2010) 352–372.
- C.P. Fredlake, J.M. Crosthwaite, D.G. Hert, S.N.V.K. Aki, J.F. Brennecke, Thermophysical Properties of Imidazolium-Based Ionic Liquids, *J. Chem. Eng. Data* 49 (2004) 954–964.
- H. Lee, S.M. Kim, T.-J. Jeon, Effects of imidazolium-based ionic liquids on the stability and dynamics of gramicidin A and lipid bilayers at different salt concentrations, *J. Mol. Graph. Model.* 61 (2015) 53–60.
- Y. Cao, R. Zhang, T. Cheng, J. Guo, M. Xian, H. Liu, Imidazolium-based ionic liquids for cellulose pretreatment: recent progresses and future perspectives, *Appl. Microbiol. Biotechnol.* 101 (2017) 521–532.
- A. Kurata, S. Shimizu, Y. Shiraiishi, M. Abe, N. Naito, M. Shimada, N. Kishimoto, Degradation of ionic liquids by a UV/H₂O₂ process and CMCase from novel ionic liquid-tolerant alkaliphilic *Nocardopsis* sp. SSC4, *Biotechnol. Biotechnol. Equip.* 31 (2017) 749–755.
- E.M. Siedlecka, W. Mroziak, Z. Kaczyński, P. Stepnowski, Degradation of 1-butyl-3-methylimidazolium chloride ionic liquid in a Fenton-like system, *J. Hazard. Mater.* 154 (2008) 893–900.
- P.A. Hunt, B. Kirchner, T. Welton, Characterising the Electronic Structure of Ionic Liquids: An Examination of the 1-Butyl-3-Methylimidazolium Chloride Ion Pair, 12 (2006) 6762–6775.
- S. Satyen, H. Satoshi, K. Akiko, H. Hiro-o, Crystal Structure of 1-Butyl-3-methylimidazolium Chloride. A Clue to the Elucidation of the Ionic Liquid Structure, 32 (2003) 740–741.
- K.-Y.-A. Lin, C.-H. Wu, A.P. Jochems, Adsorptive behaviors of methylimidazolium ionic liquids to a Y-type zeolite in water: Kinetics, isotherms, thermodynamics and interferences, *J. Mol. Liq.* 232 (2017) 269–276.
- K.-Y. Andrew Lin, C.-H. Wu, Efficient and recyclable removal of imidazolium ionic liquids from water using resorcinol–formaldehyde polymer resin, *RSC Adv.* 6 (2016) 68111–68119.
- J. Wang, J. Luo, X. Zhang, Y. Wan, Concentration of ionic liquids by nanofiltration for recycling: Filtration behavior and modeling, *Sep. Purif. Technol.* 165 (2016) 18–26.
- E. Bocos, M. Pazos, M.Á. Sanromán, Electro-Fenton treatment of imidazolium-based ionic liquids: kinetics and degradation pathways, *RSC Adv.* 6 (2016) 1958–1965.
- E.M. Siedlecka, M. Goźbiowski, J. Kumirska, P. Stepnowski, Identification of 1-Butyl-3-methylimidazolium Chloride Degradation Products Formed in Fe(III)/H₂O₂ Oxidation System, *Chem. Analytyczna*, 53 (2008) 934–951.
- A. Zawawi, R.M. Ramli, N. Yub Harun, Photodegradation of 1-Butyl-3-methylimidazolium Chloride [Bmim]Cl via Synergistic Effect of Adsorption-Photodegradation of Fe-TiO₂/AC, 5 (2017) 82.
- M. Munoz, C.M. Domínguez, Z.M. de Pedro, A. Quintanilla, J.A. Casas, J.J. Rodríguez, Ionic liquids breakdown by Fenton oxidation, *Catal. Today* 240 (2015) 16–21.
- C.M. Domínguez, M. Munoz, A. Quintanilla, Z.M. de Pedro, S.P.M. Ventura, J.A.P. Coutinho, J.A. Casas, J.J. Rodríguez, Degradation of imidazolium-based ionic liquids in aqueous solution by Fenton oxidation, *J. Chem. Technol. Biotechnol.* 89 (2014) 1197–1202.
- M. Munoz, C.M. Domínguez, Z.M. de Pedro, A. Quintanilla, J.A. Casas, S.P.M. Ventura, J.A.P. Coutinho, Role of the chemical structure of ionic liquids in their ecotoxicity and reactivity towards Fenton oxidation, *Sep. Purif. Technol.* 150 (2015) 252–256.
- M. Munoz, C.M. Domínguez, Z.M. de Pedro, A. Quintanilla, J.A. Casas, J.J. Rodríguez, Degradation of imidazolium-based ionic liquids by catalytic wet peroxide oxidation with carbon and magnetic iron catalysts, *J. Chem. Technol. Biotechnol.* 91 (2016) 2882–2887.
- S. Wang, J. Hu, J. Wang, Degradation of sulfamethoxazole using PMS activated by cobalt sulfides encapsulated in nitrogen and sulfur co-doped graphene, *Sci. Total Environ.* 827 (2022) 154379.
- S. Wang, J. Wang, Peroxymonosulfate activation by Co₉S₈@S and N co-doped biochar for sulfamethoxazole degradation, *Chem. Eng. J.* 385 (2020) 123933.
- X. Chen, J. Chen, X. Qiao, D. Wang, X. Cai, Performance of nano-Co₃O₄/peroxymonosulfate system: Kinetics and mechanism study using Acid Orange 7 as a model compound, *Appl. Catal., B* 80 (2008) 116–121.
- G.P. Anipsitakis, E. Stathatos, D.D. Dionysiou, Heterogeneous Activation of Oxone Using Co₃O₄, *J. Phys. Chem. B* 109 (2005) 13052–13055.
- W. Guo, S. Su, C. Yi, Z. Ma, Degradation of antibiotics amoxicillin by Co₃O₄-catalyzed peroxymonosulfate system, *Environ. Prog. Sustain. Energy* 32 (2013) 193–197.
- S. Wang, J. Wang, Magnetic 2D/2D oxygen doped g-C₃N₄/biochar composite to activate peroxymonosulfate for degradation of emerging organic pollutants, *J. Hazard. Mater.* 423 (2022) 127207.
- J.-Y. Lin, J. Lee, W.D. Oh, E. Kwon, Y.-C. Tsai, G. Lisak, S. Phattarapattamawong, C. Hu, K.-Y.-A. Lin, Hierarchical ZIF-decorated nanoflower-covered 3-dimensional foam for enhanced catalytic reduction of nitrogen-containing contaminants, *J. Colloid Interface Sci.* 602 (2021) 95–104.
- J.-Y. Lin, P.-Y. Chen, E. Kwon, W.D. Oh, S. You, C.-W. Huang, F. Ghanbari, T. Wi-Afedzi, K.-Y.-A. Lin, One-step synthesized 3D-structured MOF foam for efficient and convenient catalytic reduction of nitrogen-containing aromatic compounds, *J. Water Process Eng.* 40 (2021) 101933.
- X. Zhang, Y. Pan, J. Zhao, X. Hao, Y. Wang, D.W. Schubert, C. Liu, C. Shen, X. Liu, Facile Construction of Copper Mesh Surface from Superhydrophilic to Superhydrophobic for Various Oil-Water Separations, *Eng. Sci.* 7 (2019) 65–71.
- Y. Fu, A. Manthiram, Electrochemical properties of Cu₂S with ether-based electrolyte in Li-ion batteries, *Electrochim. Acta* 109 (2013) 716–719.
- M.S. Vidhya, G. Ravi, R. Yuvakkumar, P. Kumar, D. Velauthapillai, B. Saravanakumar, E.S. Babu, Cu₂S electrochemical energy storage applications, *AIP Conf. Proc.* 2270 (2020) 100011.
- V. Perumal, U. Hashim, S.C.B. Gopinath, R. Haarindraprasad, P. Poopalan, W.-W. Liu, M. Ravichandran, S.R. Balakrishnan, A.R. Ruslinda, A new nano-worm structure from gold-nanoparticle mediated random curving of zinc oxide nanorods, *Bioelectron.* 78 (2016) 14–22.
- L. Tao, X.M. Zhao, J.M. Gao, W. Hu, Lithographically defined uniform worm-shaped polymeric nanoparticles, *Nanotechnology* 21 (2010) 095301.
- S. Xu, R. Sheng, Y. Cao, J. Yan, Reversibly switching water droplets wettability on hierarchical structured Cu₂S mesh for efficient oil/water separation, *Sci. Rep.* 9 (2019) 12486.
- M. Behera, G. Giri, Green synthesis and characterization of cuprous oxide nanoparticles in presence of a bio-surfactant, *Mater. Sci.-Pol.* 32 (2014) 702–708.
- W.-J. Liu, E. Kwon, N.N. Huy, T.C. Khiem, G. Lisak, T. Wi-Afedzi, C.-C. Wu, F. Ghanbari, K.-Y.-A. Lin, Facilely-prepared sulfide-doped Co₃O₄ nanocomposite as a boosted catalyst for activating Oxone to degrade a sunscreen agent, *J. Taiwan Inst. Chem. Eng.* 133 (2022) 104253.
- X. Lv, Y. Leng, R. Wang, Y. Wei, X. Ren, W. Guo, Persulfate activation by ferrocene-based metal-organic framework microspheres for efficient oxidation of orange acid 7, *Environ. Sci. Pollut. Res.* 29 (2022) 34464–34474.
- T. Cong Khiem, X. Duan, W.-J. Liu, Y.-K. Park, H. Manh Bui, W.-D. Oh, S. Ghotekar, Y. Fai Tsang, K.-Y. Andrew Lin, MOF-templated Hollow Cobalt Sulfide as an Enhanced Oxone Activator for Degradation of UV Absorber: Key Role of Sulfur Vacancy-Induced Highly Active Coll Sites, *Chem. Eng. J.* (2022) 139699.
- Z. Jiang, W. Lu, Z. Li, K.H. Ho, X. Li, X. Jiao, D. Chen, Synthesis of amorphous cobalt sulfide polyhedral nanocages for high performance supercapacitors, *J. Mater. Chem. A* 2 (2014) 8603–8606.
- W.-J. Liu, E. Kwon, B. Xuan Thanh, T. Cong Khiem, D. Dinh Tuan, J.-Y. Lin, T. Wi-Afedzi, C. Hu, S. Sirivithayaporn, K.-Y.A. Lin, Hofmann-MOF derived nanoball assembled by FeNi alloy confined in carbon nanotubes as a magnetic catalyst

- for activating peroxydisulfate to degrade an ionic liquid, *Sep. Purif. Technol.*, 295 (2022) 120945.
- [44] C.M. Domínguez, M. Munoz, A. Quintanilla, Z.M. de Pedro, J.A. Casas, Kinetics of imidazolium-based ionic liquids degradation in aqueous solution by Fenton oxidation, *Environ. Sci. Pollut. Res.* 25 (2018) 34811–34817.
- [45] C.-Y. Hsiao, H. Wang, E. Kwon, B.X. Thanh, S. You, C. Hu, K.-Y.-A. Lin, Degradation of an imidazolium-based ionic liquid in water using monopersulfate catalyzed by Dahlia flower-like cobalt oxide, *Sep. Purif. Technol.* 274 (2021) 118668.
- [46] F. Ghanbari, A. Hassani, S. Waclawek, Z. Wang, G. Matyszczyk, K.-Y.-A. Lin, M. Dolatabadi, Insights into paracetamol degradation in aqueous solutions by ultrasound-assisted heterogeneous electro-Fenton process: Key operating parameters, mineralization and toxicity assessment, *Sep. Purif. Technol.* 266 (2021) 118533.
- [47] P.R. Gogate, A.B. Pandit, A review of imperative technologies for wastewater treatment I: oxidation technologies at ambient conditions, *Adv. Environ. Res.* 8 (2004) 501–551.
- [48] H. Herbache, A. Ramdani, Z. Taleb, R. Ruiz-Rosas, S. Taleb, E. Morallón, L. Pirault-Roy, N. Ghaffour, Catalytic degradation of O-cresol using H₂O₂ onto Algerian Clay-Na, *Water Environ. Res.* 91 (2019) 165–174.
- [49] B. Barikbin, F.S. Arghavan, A. Othmani, A. Hossein Panahi, N. Nasseh, Degradation of tetracycline in Fenton and heterogeneous Fenton like processes by using FeNi 3 and FeNi 3 /SiO 2 catalysts, *Desalin. Water Treat.* 200 (2020) 262–274.
- [50] X. Zhao, L. Liu, Y. Zhang, H. Zhang, Y. Wang, Uniquely confining Cu₂S nanoparticles in graphitized carbon fibers for enhanced oxygen evolution reaction, *Nanotechnology* 28 (2017) 345402.
- [51] Y. Pan, Y. Fang, H. Jin, M. Zhang, L. Wang, S. Ma, H. Zhu, M. Du, A Highly Active and Robust CoP/CoS₂-Based Electrocatalyst Toward Overall Water Splitting, *Electrocatalysis* 10 (2019) 253–261.
- [52] W. Wang, J. Yu, J. Zou, X. Yu, Mechanism for enhancing biodegradability of antibiotic pharmacy wastewater by in-situ generation of H₂O₂ and radicals over MnOx/nano-G/2-EAQ/AC cathode, *Electrochim. Acta* 191 (2016) 426–434.
- [53] A. Carrier, C. Nganou, D. Oakley, Y. Chen, K. Oakes, S. Macquarrie, X. Zhang, Selective Generation of Singlet Oxygen in Chloride Accelerated Copper Fenton Chemistry, 2018.
- [54] Y. Zhichao, J. Qian, A. Yu, B. Pan, Singlet oxygen mediated iron-based Fenton-like catalysis under nanoconfinement, *Proc. Natl. Acad. Sci.* 116 (2019) 201819382.
- [55] K.-Y.-A. Lin, J.-T. Lin, Ferrocene-functionalized graphitic carbon nitride as an enhanced heterogeneous catalyst of Fenton reaction for degradation of Rhodamine B under visible light irradiation, *Chemosphere* 182 (2017) 54–64.
- [56] S. Waclawek, Do We Still Need a Laboratory to Study Advanced Oxidation Processes? A Review of the Modelling of Radical Reactions used for Water Treatment, *Ecol. Chem. Eng. S* 28 (2021) 11–28.
- [57] P. Hrabák, S. Waclawek, Radical Reactions and Their Application for Water Treatment, in: J. Filip, T. Cajthaml, P. Najmanová, M. Černík, R. Zbořil (Eds.), *Advanced Nano-Bio Technologies for Water and Soil Treatment*, Springer International Publishing, Cham, 2020, pp. 203–219.
- [58] S.G. Pati, W.A. Arnold, Reaction rates and product formation during advanced oxidation of ionic liquid cations by UV/peroxide, UV/persulfate, and UV/chlorine, *Environ. Sci.: Water Res. Technol.* 4 (2018) 1310–1320.